THE JOURNAL OF PHYSICAL CHEMISTRY A

Article

pubs.acs.org/JPCA

Phase Controlled Homodyne Infrared Near-Field Microscopy and Spectroscopy Reveal Inhomogeneity within and among Individual Boron Nitride Nanotubes

Xiaoji G. Xu, Adrienne E. Tanur, and Gilbert C. Walker*

Department of Chemistry, University of Toronto, Toronto, Ontario, M5S 3H6, Canada

Supporting Information

ABSTRACT: We propose a practical method to obtain near-field infrared absorption spectra in apertureless near-field scanning optical microscopy (*a*NSOM) through homodyne detection with a specific choice of reference phase. The underlying mechanism of the method is illustrated by theoretical and numeric models to show its ability to obtain absorptive rather than dispersive profiles in near-field infrared vibrational microscopy. The proposed near-field nanospectroscopic method is applied to obtain infrared spectra from regions of individual multiwall boron nitride nanotubes (BNNTs) in spatial regions smaller than the diffraction limit of the light source. The spectra suggest variations in interwall spacing within the individual tubes probed.

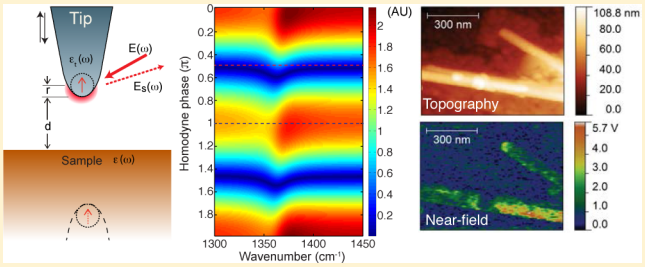

INTRODUCTION

Routine vibrational spectroscopy of nanoscale materials is a huge challenge in nanosciences. Far-field spectroscopies are hampered by the diffraction limit of light; i.e., the spatial resolution cannot exceed one-half of the light wavelength that is characteristic of far-field spectroscopies.[1] The diffraction-limited spatial resolution for infrared light is typically a few micrometers, which is much larger than many interesting objects such as nanoparticles and nanotubes. The difficulty of imaging individual nano-objects in vibrational spectroscopy leads to the spatial averaging of multiple objects, which contributes to spectral inhomogenous broadening in FTIR and Raman spectra.[2] Utilization of near-field methods provides a solution for moving beyond the diffraction limit.[1,3−7] Apertureless near-field scanning optical microscopy (*a*NSOM) enables high spatial resolution through local light scattering,[8−11] and when combined with infrared light sources, *a*NSOM provides a promising approach.[12−18]

Scattering type IR *a*NSOM generates a detectable signal by light scattering from a sharp tip in proximity to polarizable samples,[19] while traditional infrared absorption spectroscopy measures the extinction of light that passes through samples.[20] The spectrum of the scattered light does not typically exhibit an absorptive profile but rather shows a dispersive profile.[21] Dispersive profiles are hard to interpret and lack a simple correspondence to existing infrared vibrational spectral data banks. This problem of dispersive profiles can be overcome by measuring the spectral phase via the frequency domain technique of pseudo-heterodyne detection.[22,23] Another complementary method is to measure an asymmetric interferogram with near-field scattering light and a reference and then perform a Fourier transform.[15,17,18] In particular, the frequency domain method of pseudo-heterodyne detection allows one to directly read out the spectral phase of the sample response, which was found to resemble absorption spectra.[23] The time domain method measures asymmetric interferograms and obtains the imaginary part,[17] or the spectral phase[18] of the near-field response through a Fourier transform. However, pseudo-heterodyne methods require a special double modulation scheme and a somewhat complex harmonic analysis, whereas the time domain method requires expensive light sources and suffers from low spectral irradiance despite using the current state-of-the-art instrumentation.

In this article, we report a conceptually simple and yet effective frequency domain method for obtaining the near-field absorption profile with IR *a*NSOM by precise, controlled homodyne. We then utilize it to explore the unchartered territory of spectroscopic investigation of intratube inhomogeneity among and within individual boron nitride nanotubes (BNNTs).[24]

BNNTs are structurally similar to carbon nanotubes and have a similar mechanical applications.[25,26] BNNTs can be visualized in a similar fashion to carbon nanotubes, as the wrapping of hexagonal boron nitride (*h*-BN) sheet into a tube. However, in contrast to carbon nanotubes, BNNTs are insulators; in addition, they possess a higher resistance to oxidization and can withstand high temperatures, making them a promising replacement material for carbon nanotubes under such adverse environments. BNNTs are being developed as fillers for composite materials such as encapsulants and biomaterials[27]

Received: January 25, 2013
Revised: March 1, 2013
Published: March 6, 2013

dx.doi.org/10.1021/jp4008784 | *J. Phys. Chem. A* 2013, 117, 3348−3354

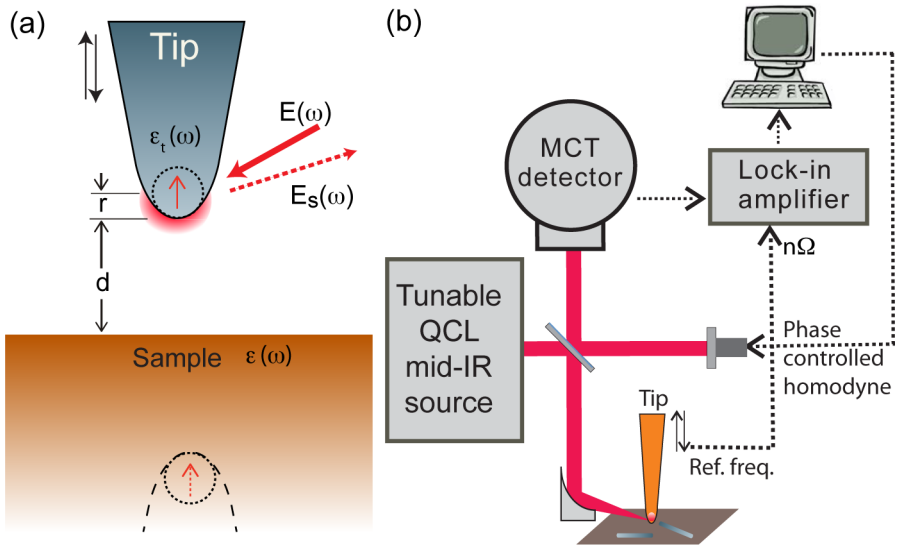

Figure 1. (a) Illustration of the image dipole approximation. The sample surface forms an image dipole according to its dielectric function $\varepsilon(\omega)$. The tip performs tapping motions above the sample, undergoing harmonic oscillation. (b) Scheme of the homodyne interferometric IR *a*NSOM apparatus that is used in the experiment. It includes an IR light source, an asymmetric Michelson interferometer, an atomic force microscope, and lock-in detection of the signal.

and are candidate materials for optoelectronic devices with novel magnetic and electronic properties.[27−29] Unlike carbon nanotubes, BNNTs exhibit polar features, with boron atoms possessing a partial positive charge and nitrogen atoms having a partial negative charge.[30] As a result, a number of BNNT phonon modes are strongly infrared active. Unlike the sp^2 orbital hybridization of carbon in graphite, nitrogen atoms in *h*-BN have a partial sp^3 orbital hybridization, which leads to out of plane buckling of negatively charged nitrogen and positively charged boron atoms above and below the plane of the *h*-BN sheet, which in turn leads to a dipole distribution above and below each sheet. Consequently, long-range dipole−dipole interaction between adjacent *h*-BN sheets leads to a splitting between longitudinal and transverse phonon modes (LO−TO splitting[30]) of 1370 and 1510 cm^{-1} frequencies. In a BNNT such mode splitting leads to a shift of the vibrational frequency and is spectrally indicative of interwall distances in multiwall BNNTs. For single wall BNNT, infrared spectra depend on the tube diameter and chirality.[30,31] Near-field infrared nanospectroscopy enables such structural studies within tubes. BNNTs exhibit high thermal conductivity[32] and a band gap[33] that is unusually strongly coupled to vibrational strain resulting in a poorly understood decrease in performance as a field effect transistor material.[34] Vibrational spectroscopic studies within single nanotubes have the potential to assist in screening for superior materials by identifying defects.[24,35,36]

THEORY AND SIMULATION

The theoretical treatment for near-field scattering in *a*NSOM is described using the image dipole approximation.[19,37−39] A sharp metal coated scanning probe tip acts as an induced dipole under the incident optical field (Figure 1a). The induced dipole induces charge distributions at a sample surface, which can be mathematically treated as an effective image dipole rectifying the electric field of the induced dipole of the metallic tip. The effective polarizability of the metallic tip in proximity to the sample is given by the effective polarizability eq 1.

$$\alpha_{\text{eff}}(\omega) = \alpha\left(1 - \frac{\alpha\beta}{16\pi(r+d)^3}\right)^{-1} \quad (1)$$

where r is the tip apex radius and d is the tip−sample distance. α is the uncoupled tip polarizability in free space with $\alpha = 4\pi r^3(\varepsilon_t - 1)/(\varepsilon_t + 2)$. $\beta = (\varepsilon(\omega) - 1)/(\varepsilon(\omega) + 1)$ is the coefficient found to satisfy the Maxwell equations. ε_t is the dielectric function of the tip, and $\varepsilon(\omega)$ is the dielectric function of the sample, which is frequency dependent.

The image dipole approximation provides a quantifiable model for elaborate numeric simulations of the near-field scattering mechanism. One key discussion in near-field nanospectroscopy is the role of vibrational resonance in the sample in near-field scattering. Vibrational resonances in molecules retain image dipole polarization after laser excitations, which in the frequency domain corresponds to a phase shift around the frequency of resonance. Such a phase shift leads to redistribution of the polarization amplitude between the real and imaginary parts of the effective polarizability, and the strength of such redistribution depends on the tip−sample distance d. Figure 2a and Figure 2b show the real and imaginary parts of the simulated effective polarizability α_{eff} when the tip is nearly in contact with the surface (red, $d = 0.01r$) and when it is retracted by one tip radius (blue, $d = r$) for a sample containing a boron nitride vibrational resonance. There are two relevant features of this comparison. First, the real part outweighs the imaginary part by two orders of magnitude, even when the tip is in proximity to the sample. As a result, the overall profile of near-field scattered light would assume the dispersive profile of the real part. Second, the imaginary part of α_{eff}, although quite small compared to the real part, has the profile corresponding to the absorptive profile of the sample.[19,14] This is because the sample has the ability to retain polarization after exposure to the excitation field, and this elongation of the time domain polarization is determined by the near-field absorptive profile of the sample and contributes to the imaginary part of the polarizability. Note that such a profile correspondence between the absorption spectra and the

dx.doi.org/10.1021/jp4008784 | J. Phys. Chem. A 2013, 117, 3348−3354

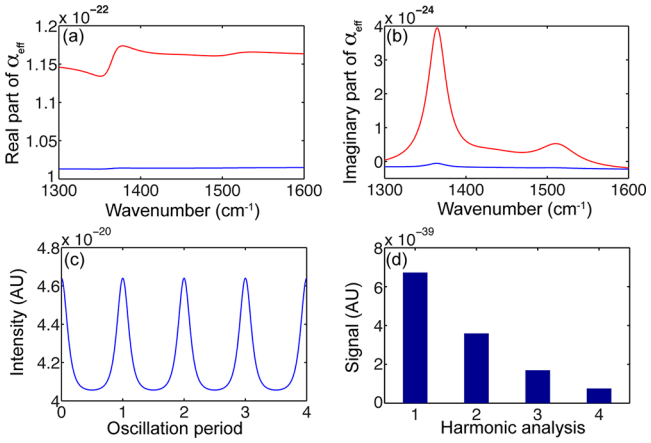

Figure 2. (a) Real part of the effective polarizability $\alpha_{eff}(\omega)$ of the tip and sample. The dielectric function used in this simulation is estimated from a typical FTIR spectrum of BNNT.[26] The real part exhibits a dispersive profile and non-zero values. (b) Imaginary part of $\alpha_{eff}(\omega)$ under the same conditions as (a). (c) Simulated total tip sample scattered intensity as a function of tip oscillation periods. (d) Fourier analysis of the modulation of scattered intensity showing contributions from both the fundamental and higher harmonics of the tip oscillation frequency. It simulates lock-in detection in *a*NSOM.

imaginary part of the tip sample polarizability can be derived from linear response theory by treating the tip sample polarizability α_{eff} as a response function $\alpha_{eff}(\omega)$. Therefore, even for theoretical models beyond a simple image dipole,[40] the correspondence between the imaginary part and the dissipative absorptive profile should still hold.

The scattered light has the same frequency as the incident light, and therefore, *a*NSOM requires vertical tip oscillatory motions to modulate the light scattering in order to enhance the detection of the near-field contribution.[10] Figure 2c shows the intensity of the scattered light $|\alpha_{eff}E(\omega)|^2$ as a function of the tip oscillation period. Near-field enhancement leads to an increase of the scattered light when the tip is close to the sample, which creates an anharmonic waveform of scattered intensity. A Fourier analysis of the scattered waveform gives harmonic and higher harmonic components of the scattered light (Figure 2d). Higher harmonic components correspond more closely to the near-field scattering than does the fundamental (first) harmonic component. In the *a*NSOM experiment, a lock-in amplifier performs the function of Fourier analysis via demodulation at the tip vertical oscillation frequency. In the following numeric simulations, we perform Fourier analysis on our numerically generated signal to simulate lock-in readout of the second harmonic demodulation.

In the *a*NSOM experiment, the scattered field is homodyned with a large magnitude reference optical field that is often from the same laser source.[37,41] The homodyne method is phase sensitive. The homodyned signal detected by the square law detector is shown in eq 2, where A and ϕ are the amplitude and phase of the reference optical field.

$$I_s(\omega) = |\alpha_{eff}E(\omega) + A\,e^{i\phi}E(\omega)|^2 \quad (2)$$

Equation 2 can be recast into an expression with the imaginary and real parts of α_{eff} in eq 3.

$$I_s(\omega) = ((\mathrm{Re}\{\alpha_{eff}\} + A\cos\phi)^2 + (\mathrm{Im}\{\alpha_{eff}\} + A\sin\phi)^2)\,|E(\omega)|^2 \quad (3)$$

By tuning the phase ϕ of the homodyne optical field, one can selectively amplify the real or imaginary component of α_{eff}.

We then simulate lock-in detection of the homodyned light scattered spectrum by changing ϕ. The $\phi = 0$ phase is defined as the phase of near-field scattered light from the metal (gold) substrate that does not contain any detectable vibrational or phonon resonance. Similarly, $\phi = \pi$ corresponds to the phase of light that is delayed by a half wavelength of optical path. Figure 3a shows the numeric simulation of the homodyned near-field

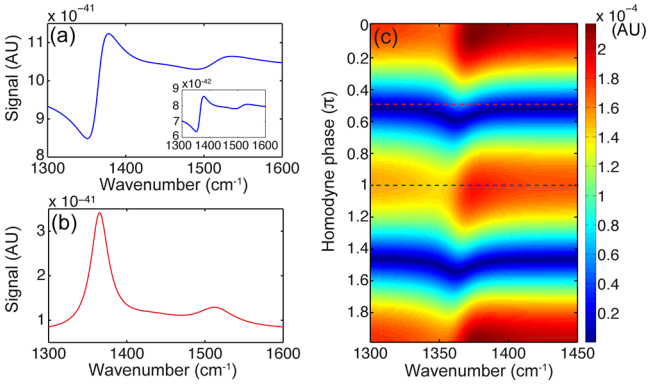

Figure 3. (a) Plot of the simulated homodyned spectrum of near-field scattering, with the homodyne phase of reference field set to $\phi = 0$. Inset shows the nonhomodyned spectrum. (b) Plot of simulated homodyned spectrum, with reference field tuned to $\pi/2$. (c) Simulated two-dimensional plot showing the homodyned spectra as a function of homodyne phase. The $\pi/2$ and π phase settings are marked by a dashed line, which correspond to the absorptive and dispersive profiles shown in (b) and (a).

spectrum light where A is 10 times as large as $|\alpha_{eff}|$ and $\phi = 0$. The figure shows the optical frequency dependence of the second harmonic component of the Fourier analysis on the simulated waveform with the tip tapping on the sample. The $\phi = 0$ phase amplifies the real part of the scattered light, which corresponds to an optical path difference between two interferometer arms that is an integer multiple of the light wavelength. The inset of Figure 3a shows the absolute amplitude of the scattered light, which has a dispersive profile before the homodyne amplification. Figure 3b shows the same homodyne condition but with phase ϕ tuned to $\pi/2$. In contrast, it amplifies the imaginary part of the effective polarizability α_{eff} and reveals the absorption spectrum. A two-dimensional pseudo color plot shows the homodyned spectra as a function of the homodyne phase ϕ varying from 0 to 2π (Figure 3c). It can be seen in Figure 3c that when ϕ equals an odd multiple of $\pi/2$, the homodyned near-field spectrum after lock-in demodulation gives absorptive profiles, while when ϕ equals an even multiple of $\pi/2$, the homodyned near-field spectrum after lock-in demodulation gives dispersive profiles. It is notable that the homodyne detection of the maximizing signal on the sample or substrate typically leads to dispersive profiles. The $\pi/2$ phase, on the other hand, does not give the highest amount of total signal but efficiently extracts the valuable imaginary part of the near-field signal, which corresponds to the absorptive profile of the vibrational resonances. The $\pi/2$ phase also corresponds to the minimum signal generated from an off-resonant or nonresonant sample/substrate. This feature provides a practical way of fulfilling the $\pi/2$ requirement in the subsequent experimental studies by

dx.doi.org/10.1021/jp4008784 | J. Phys. Chem. A 2013, 117, 3348−3354

minimizing the lock-in demodulated signal from a nonresonant substrate.

EXPERIMENTAL METHOD

We apply the method described above for individual BNNT identification using information about the transverse optical E_{1u} vibrational mode (~1370 cm^{-1})[42] of *h*-BN.[30,31,43] The sample is synthesized by growth vapor trapping chemical vapor deposition (GVT-CVD) as previously described.[26,44] The sample is sonicated for 30 min in ethanol and drop-casted onto a gold substrate.

The experimental near-field setup is shown in Figure 1b. A quantum cascade laser (QCL, Daylight Solutions) is used to provide a frequency tunable, continuous wave, mid-infrared source of 100 mW average power. An asymmetric Michelson interferometer is built with a 50:50 IR beam splitter (Edmund Optics). One-half of the light is focused on the tip apex of a modified atomic force microscope (Multimode AFM, Digital Instruments) by a 90° off-axis gold coated parabolic mirror (f = 50 mm). The AFM operates in tapping mode with platinum coated tips (DPE 14 Mikromash) driven at $\Omega \simeq 137$ kHz. The tip-scattered infrared light is homodyned by a phase controlled reference beam and detected by a mercury cadmium telluride (MCT) detector (J15D12 Teledyne-Judson). The near-field contribution is extracted by a lock-in amplifier (SRS 844, Stanford Research Systems) demodulated at the third harmonic of the tip oscillation frequency (3Ω, 3 ms time constant) using a customized reference frequency tripling circuit. The mid-infrared laser field is polarized parallel to the tip axis for efficient excitation of the tip dipole.[45] The $\pi/2$ homodyne phase is set by minimizing the third harmonic signal when the tip is scanning above the gold substrate adjacent to where the BNNTs are deposited. Chemically sensitive images based on near-field absorption profiles are recorded with frequency tuning across the vibrational resonances of BNNT. A nanospectrum is constructed using intensities from the images collected at different laser frequencies.

RESULTS AND DISCUSSION

Individual BNNTs are studied spectroscopically. Figure 4a and Figure 4b show AFM topography and phase scans of two strands of BNNTs on a gold substrate. They have diameters of ~60 nm. The IR *a*NSOM imaging maps are shown in Figure 4c,f with the IR wavelength tuned to 1353, 1371, 1402, and 1422 cm^{-1}, respectively, with the homodyne phase set to $\pi/2$ by the above-mentioned procedure (for an *a*NSOM scan with homodyne in-phase, see Supporting Information). These images contain rich information on the variation of structural composition within BNNTs that cannot be provided by either AFM topography or AFM phase imaging. The controlled $\pi/2$ phase homodyne allows background free detection when the sample does not contain a vibrational resonance as shown in *a*NSOM image at 1353 cm^{-1}. At 1371 cm^{-1}, the chemical sensitive *a*NSOM image (Figure 4d) reveals that both BNNTs contains vibrations resonant at this frequency. Nonresonant contaminations attached to the BNNT (marked by circles in Figure 4a) do not show near-field signal at this frequency.

At 1402 cm^{-1}, the right side of the lower tube (labeled as tube 2) shows a stronger *a*NSOM signal under the $\pi/2$ phase homodyne compared with the upper tube (labeled as tube 1) and left side of the lower tube (labeled as tube 3). The image at this frequency reveals structural variation along tube 2 as well.

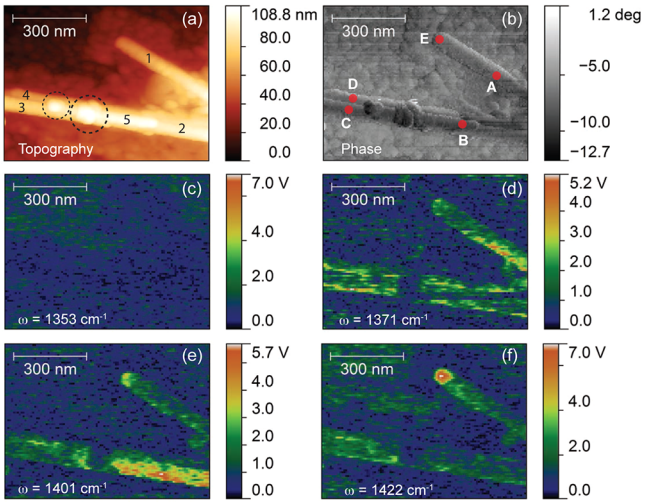

Figure 4. (a) AFM topographic image of two BNNTs labeled as upper tube 1 and lower tube 2. (b) AFM phase image of two corresponding BNNTs. (c) IR *a*NSOM vibrational imaging using $\pi/2$ phase homodyne of BNNT at 1353 cm^{-1}, (d) BNNTs at 1371 cm^{-1}, (e) BNNTs at 1401 cm^{-1}, and (f) BNNTs at 1422 cm^{-1}.

The topography (Figure 4a) indicates that the right to middle side of the lower tube is actually a bundle consisting of multiple smaller tubes (labeled as subtubes 3, 4, and 5). Comparable near-field intensity on the vibrational sensitive *a*NSOM imaging at this infrared frequency suggests that subtube 5 and tube 2 are of similar BNNT structure while tube 1 and subtube 3 are the same. Even though subtube 3 and subtube 4 are close to each other, their structures are different if we assume their chemical compositions are similar.

When the laser is tuned to 1422 cm^{-1}, an interesting feature is observed at the terminal end of tube 1, as shown in Figure 4f). The strong *a*NSOM signal under $\pi/2$ phase homodyne at the terminal end likely indicates a different BNNT structure. An apparently less constrained structure is found at the tube terminal compared with the tube shaft, i.e., a larger separation between constituent BN layers than the tube shaft, which corresponds to a weakened LO−TO splitting. As a result, the transverse optical mode shifts to higher frequency as indicated by the near-field spectroscopic observation. To further investigate intratube inhomogeneities, we studied another BNNT of different size with *a*NSOM vibrational sensitive imaging. Figure 5 shows AFM topography (a), phase image (b), and *a*NSOM vibrational sensitive images at 1397 cm^{-1} (c) and 1418 cm^{-1} (d) of a long BNNT. The AFM topography image provides the dimensions of the BNNT, and the *a*NSOM vibrational imaging reveals variations in near-field absorption along the tube. In particular, at 1418 cm^{-1}, two near-field absorption nodes along the BN nanotube are identified. The location of the upper left node coincides with a small shape variation on the AFM topography image (marked by a dashed circle in Figure 5a and Figure 5b), whereas the location of the lower right node is not identifiable from either the AFM topography or phase images. Following the same model of LO−TO splitting, such spectral variations can be explained by the spacing variations between the walls of a BNNT. Figure 5e shows an *a*NSOM intensity profile comparison between 1397 and 1418 cm^{-1} along the BNNT shown in Figure 5a−d). The profile shows an anticorrelation of intensity at these two frequencies, which further support that the localized variations

dx.doi.org/10.1021/jp4008784 | J. Phys. Chem. A 2013, 117, 3348−3354

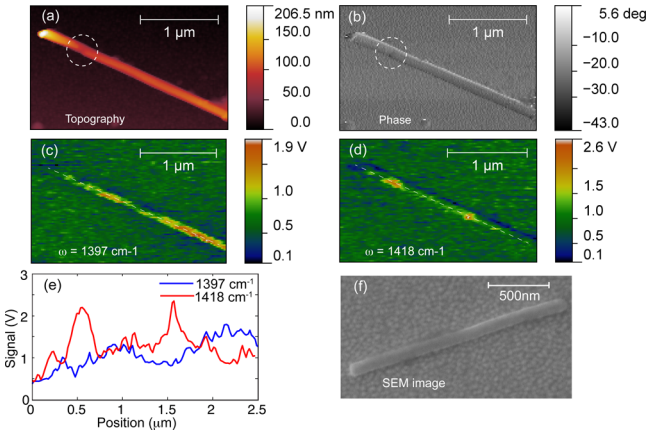

Figure 5. (a) AFM topography image of a long BNNT. (b) AFM phase image of this BNNT. (c) IR *a*NSOM vibrational imaging using $\pi/2$ phase homodyne of the BNNT at 1397 cm^{-1} and (d) at 1418 cm^{-1}. (e) Profile extraction from IR *a*NSOM vibrational imaging along the tube shown in (c) and (d), marked by white dashed lines. (f) SEM image of a typical BNNT (it is from the same BNNT sample, but it is a different tube).

are due to BNNT structural differences. Such structural changes may be related to helicity changes due to defects, missing tubular layers, and structural twists[35] that are not always correlated with external topography. Spatial mapping of structural variations[46] should provide information for the elucidation of the BNNT growth mechanism, and we speculate that the spectral modulations along the tube may reflect non-uniform growth of the tube caused by a fluctuating catalyst particle.[47,48] A scanning electron microscope (SEM) image of a typical BNNT is shown in Figure 5f. The SEM image reveals a noticeable but very small image contrast along the tube, which hints at structural variations within the BNNT.[49] On the other hand, the near-field vibrational imaging based on near-field absorption provides a direct and novel measurement of BNNT structural variation.

To demonstrate the nanospectroscopy capability of the $\pi/2$ phase homodyne approach, we tuned our quantum cascade laser from 1350 to 1431 cm^{-1} to obtain multiple *a*NSOM images at different frequencies from the smaller area of BNNTs shown in Figure 4. Extraction of near-field intensities from multiple IR *a*NSOM images with $\pi/2$ phase homodyne allows construction of near-field IR absorption spectra at different locations on the BNNTs. The *a*NSOM intensities from the gold substrate under in-phase homodyne at corresponding frequencies are recorded and used to normalize the spectrum. Absorption spectra at positions A–E from BNNTs (marked in Figure 4b) are shown in Figure 6a–e. The near-field intensity is normalized by the scattering intensity from the gold substrate with in-phase scattering by the gold substrate. At location A on tube 1, there is a vibrational resonance centered at 1380 cm^{-1} with a fwhm of about 15 cm^{-1} and a broad resonant band extended to higher frequencies. At location B on tube 2, in addition to the vibrational peak near 1380 cm^{-1} there is also a strong vibrational resonance centered at 1408 cm^{-1} with a fwhm of about 20 cm^{-1}. The spectrum at location C exhibits similarity with location A, suggesting a similar BN structure in tube 1 and subtube 3. The spectrum at location D bears

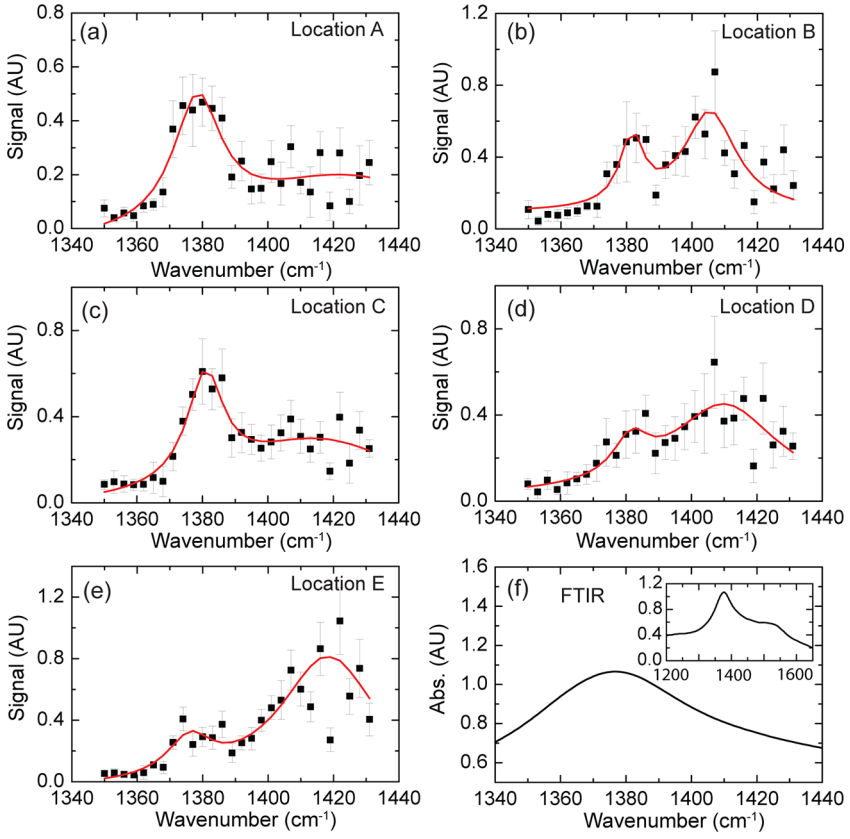

Figure 6. (a–e) Extracted nano-IR spectrum from location A to location E marked in Figure 4b. (f) Far-field FTIR spectrum of BNNT powders of the same sample batch over the same frequency range. Inset shows a FTIR spectrum of a wider range.

dx.doi.org/10.1021/jp4008784 | J. Phys. Chem. A 2013, 117, 3348–3354

resemblance to that at location B, suggesting that subtubes 3 and 5 have similar structures. Despite the spatial proximity of only 60 nm, location C and location D exhibit different spectra. Locations C and D correspond to subtubes 3 and 4, which constitute one bundle of BNNTs. The observation of spectral variation between tubes may explain the origin of mechanical property variations among BNNTs as previously oberved.[26] The spectrum at location E (at a tube terminal) exhibits a strong blue-shifted absorptive peak around 1420 cm^{-1} in addition to the common absorptive resonance around 1380 cm^{-1} from the same tube. Emergence of both 1380 and 1400 cm^{-1} resonant peaks from one individual BNNT suggests that (a) at least three coaxial tubes constitute the multiwall BNNT *and* (b) the interwall distances differ along the tube.

There are significant differences in the infrared spectra both between BNNTs and within an individual BNNT, as revealed by phase controlled homodyne near-field nanospectroscopy. An FTIR spectrum of bulk BNNT powder from the same sample used in the *a*NSOM measurement is shown in Figure 6d, which corresponds to an average of spectra of millions to billions of individual nanotubes. The far-field spectrum shows a broad absorption band more than 80 cm^{-1} wide. The spectra of BNNTs from the near-field measurement are within the frequency range of the far-field band and can be considered as contributions to the spatially averaged FTIR spectrum. Conceptually, this is an example of near-field nanospectroscopy solving the spatially averaged inhomogeneous broadening phenomenon that is characteristic of far-field FTIR.

SUMMARY AND PROSPECTIVE

Our vibrational sensitive imaging on BNNTs reveals intertube and intratube inhomogeneity corresponding to structural variation. The infrared nanospectra of BNNTs are obtained based on the absorptive profile of the sample, with a specific choice of $\pi/2$ homodyne phase in interferometric *a*NSOM. With the phase controlled homodyne condition, we are able to perform nanospectroscopy on individual BNNTs that are adjacent to one another (<20 nm spatial resolution; see Supporting Information). Our measurement provides an example of resolving inhomogeneous broadening from spatial averaging. In this regard, near-field nanospectroscopy is a method that complements two-dimensional infrared spectroscopy.[20] For instance, by use of two-dimensional IR spectroscopy to obtain the homogeneous line width, it is feasible to further quantify the intratube and intertube contributions to the inhomogeneous broadening of the IR spectrum. Compared with the pseudo-heterodyne method, this $\pi/2$ homodyne method is susceptible to larger noise due to drift of the homodyne reference phase, but it allows for faster data acquisition.[50] Further development of the proposed method would involve improvement of the homodyne phase stability: for example, implementation of a feedback mechanism to actively stabilize the optical path difference between the Michelson interferometer arms in *a*NSOM. In terms of further studies of BNNT with IR *a*NSOM, one further measurement will be to study intratube inhomogeneity to establish a correlation between tube morphology and spectral signatures. In the sister field of research of condensed phase matter physics, implementation of $\pi/2$ homodyne to extract the imaginary part of the near-field polarizability can be used to map the dissipative part of conductivity at mid-infrared frequencies on the nanometer scale for spatially inhomogeneous materials.

ASSOCIATED CONTENT

Supporting Information

Information on spatial resolution of *a*NSOM, comparison of in-phase homodynes, and *a*NOM image of a bent nanotube. This material is available free of charge via the Internet at http://pubs.acs.org.

AUTHOR INFORMATION

Corresponding Author

*E-mail: gwalker@chem.utoronto.ca.

Notes

The authors declare no competing financial interest.

ACKNOWLEDGMENTS

We thank Dr. Gregory Andreev for insightful suggestions. We thank NSERC for funding this research.

REFERENCES

(1) Betzig, E.; Trautman, J. K. Near-field Optics—Microscopy, Spectroscopy and Surface Modification beyond the Diffraction Limit. *Science* **1992**, *257*, 189−195.

(2) Levin, I. W.; Bhargava, R. Fourier Transform Infrared Vibrational Spectroscopic Imaging: Integrating Microscopy and Molecular Recognition. *Annu. Rev. Phys. Chem.* **2005**, *56*, 429−474.

(3) Durig, U.; Pohl, D. W.; Rohner, F. Near-Field Optical Scanning Microscopy. *J. Appl. Phys.* **1986**, *59*, 3318−3327.

(4) Zenhausern, F.; Martin, Y.; Wickramasinghe, H. K. Scanning Interferometric Apertureless Microscopy—Optical Imaging at 10 Angstrom Resolution. *Science* **1995**, *269*, 1083−1085.

(5) Hartschuh, A.; Sanchez, E. J.; Xie, X. S.; Novotny, L. High-Resolution Near-Field Raman Microscopy of Single-Walled Carbon Nanotubes. *Phys. Rev. Lett.* **2003**, *90*, 095503.

(6) Novotny, L.; Stranick, S. J. Near-Field Optical Microscopy and Spectroscopy with Pointed Probes. *Annu. Rev. Phys. Chem.* **2006**, *57*, 303−331.

(7) Paulite, M.; Blum, C.; Schmid, T.; Opilik, L.; Eyer, K.; Walker, G. C.; Zenobi, R. Full Spectroscopic Tip-Enhanced Raman Imaging of Single Nanotapes Formed from β-Amyloid(1-40) Peptide Fragments. *ACS Nano* **2013**, *7*, 911−920.

(8) Inouye, Y.; Kawata, S. Near-Field Scanning Optical Microscope with a Metallic Probe Tip. *Opt. Lett.* **1994**, *19*, 159−161.

(9) Knoll, B.; Keilmann, F. Scanning Microscopy by Mid-Infrared Near-Field Scattering. *Appl. Phys. A: Mater. Sci. Process.* **1998**, *66*, 477−481.

(10) Knoll, B.; Keilmann, F. Near-Field Probing of Vibrational Absorption for Chemical Microscopy. *Nature* **1999**, *399*, 134−137.

(11) Akhremitchev, B. B.; Pollack, S.; Walker, G. C. Apertureless Scanning Near-Field Infrared Microscopy of a Rough Polymeric Surface. *Langmuir* **2001**, *17*, 2774−2781.

(12) Brehm, M.; Taubner, T.; Hillenbrand, R.; Keilmann, F. Infrared Spectroscopic Mapping of Single Nanoparticles and Viruses at Nanoscale Resolution. *Nano Lett.* **2006**, *6*, 1307−1310.

(13) Cvitkovic, A.; Ocelic, N.; Hillenbrand, R. Material-specific Infrared Recognition of Single Sub-10 nm Particles by Substrate-enhanced Scattering-type Near-field Microscopy. *Nano Lett.* **2007**, *7*, 3177−3181.

(14) Mueller, K.; Yang, X. J.; Paulite, M.; Fakhraai, Z.; Gunari, N.; Walker, G. C. Chemical Imaging of the Surface of Self-Assembled Polystyrene-*b*-poly(methyl methacrylate) Diblock Copolymer Films Using Apertureless Near-Field IR Microscopy. *Langmuir* **2008**, *24*, 6946−6951.

(15) Amarie, S.; Keilmann, F. Broadband-Infrared Assessment of Phonon Resonance in Scattering-Type Near-Field Microscopy. *Phys. Rev. B* **2011**, *83*, 045404.

(16) Amarie, S.; Zaslansky, P.; Kajihara, Y.; Griesshaber, E.; Schmahl, W. W.; Keilmann, F. Nano-FTIR Chemical Mapping of Minerals in Biological Materials. *Beilstein J. Nanotechnol.* **2012**, *3*, 312−323.
(17) Huth, F.; Govyadinov, A.; Amarie, S.; Nuansing, W.; Keilmann, F.; Hilenbrand, R. Nano-FTIR Absorption Spectroscopy of Molecular Fingerprints at 20 nm Spatial Resolution. *Nano Lett.* **2012**, *12*, 3973−3978.
(18) Xu, X. G.; Rang, M.; Craig, I. M.; Raschke, M. B. Pushing the Sample-Size Limit of Infrared Vibrational Nanospectroscopy: From Monolayer toward Single Molecule Sensitivity. *J. Phys. Chem. Lett.* **2012**, *3*, 1836−1841.
(19) Knoll, B.; Keilmann, F. Enhanced Dielectric Contrast in Scattering-Type Scanning Near-Field Optical Microscopy. *Opt. Commun.* **2000**, *182*, 321−328.
(20) Hamm, P.; Zanni, M. T. *Concepts and Methods of 2D Infrared Spectroscopy*; Cambridge University Press: Cambridge, U.K., 2011.
(21) Taubner, T.; Hillenbrand, R.; Keilmann, F. Nanoscale Polymer Recognition by Spectral Signature in Scattering Infrared Near-Field Microscopy. *Appl. Phys. Lett.* **2004**, *85*, 5064−5066.
(22) Ocelic, N.; Huber, A.; Hillenbrand, R. Pseudoheterodyne Detection for Background-Free Near-Field Spectroscopy. *Appl. Phys. Lett.* **2006**, *89*, 101124.
(23) Stiegler, J. M.; Abate, Y.; Cvitkovic, A.; Romanyuk, Y. E.; Huber, A. J.; Leone, S. R.; Hillenbrand, R. Nanoscale Infrared Absorption Spectroscopy of Individual Nanoparticles Enabled by Scattering-Type Near-Field Microscopy. *ACS Nano* **2011**, *5*, 6494−6499.
(24) Golberg, D.; Bando, Y.; Huang, Y.; Terao, T.; Mitome, M.; Tang, C. C.; Zhi, C. Y. Boron Nitride Nanotubes and Nanosheets. *ACS Nano* **2010**, *4*, 2979−2993.
(25) Golberg, D.; Costa, P.; Lourie, O.; Mitome, M.; Bai, X. D.; Kurashima, K.; Zhi, C. Y.; Tang, C. C.; Bando, Y. Direct Force Measurements and Kinking under Elastic Deformation of Individual Multiwalled Boron Nitride Nanotubes. *Nano Lett.* **2007**, *7*, 2146−2151.
(26) Tanur, A. E.; Wang, J.; Reddy, A. L. M.; Lamont, D. L.; Yap, Y. K.; Walker, G. C. Diameter-Dependent Bending Modulus of Individual Multiwall Boron Nitride Nanotubes. *J. Phys. Chem. C* [Online early access]. DOI: 10.1021/jp308893s. Published Online: Dec 19 **2012**.
(27) Golberg, D.; Bando, Y.; Tang, C. C.; Zhi, C. Y. Boron Nitride Nanotubes. *Adv. Mater.* **2007**, *19*, 2413−2432.
(28) Terrones, M.; Charlier, J. C.; Gloter, A.; Cruz-Silva, E.; Terres, E.; Li, Y. B.; Vinu, A.; Zanolli, Z.; Dominguez, J. M.; Terrones, H.; Bando, Y.; Golberg, D. Experimental and Theoretical Studies Suggesting the Possibility of Metallic Boron Nitride Edges in Porous Nanourchins. *Nano Lett.* **2008**, *8*, 1026−1032.
(29) Bai, X. D.; Golberg, D.; Bando, Y.; Zhi, C. Y.; Tang, C. C.; Mitome, M.; Kurashima, K. Deformation-Driven Electrical Transport of Individual Boron Nitride Nanotubes. *Nano Lett.* **2007**, *7*, 632−637.
(30) Wirtz, L.; Rubio, A.; de la Concha, R. A.; Loiseau, A. Ab initio Calculations of the Lattice Dynamics of Boron Nitride Nanotubes. *Phys. Rev. B* **2003**, *68*, 045425.
(31) Arenal, R.; Ferrari, A. C.; Reich, S.; Wirtz, L.; Mevellec, J. Y.; Lefrant, S.; Rubio, A.; Loiseau, A. Raman Spectroscopy of Single-Wall Boron Bitride Nanotubes. *Nano Lett.* **2006**, *6*, 1812−1816.
(32) Zhi, C. Y.; Xu, Y. B.; Bando, Y.; Golberg, D. Highly Thermo-Conductive Fluid with Boron Nitride Nanofillers. *ACS Nano* **2011**, *5*, 6571−6577.
(33) Li, X. L.; Wu, X. J.; Zeng, X. C.; Yang, J. L. Band-Gap Engineering via Tailored Line Defects in Boron-Nitride Nanoribbons, Sheets, and Nanotubes. *ACS Nano* **2012**, *6*, 4104−4112.
(34) Ghassemi, H. M.; Lee, C. H.; Yap, Y. K.; Yassar, R. S. Field Emission and Strain Engineering of Electronic Properties in Boron Nitride Nanotubes. *Nanotechnology* **2012**, *23*, 105702.
(35) Golberg, D.; Mitome, M.; Bando, Y.; Tang, C.; Zhi, C. Multi-Walled Boron Nitride Nanotubes Composed of Diverse Cross-Section and Helix Type Shells. *Appl. Phys. A: Mater. Sci. Process.* **2007**, *88*, 347−352.
(36) Liu, Y. Y.; Zou, X. L.; Yakobson, B. I. Dislocations and Grain Boundaries in Two-Dimensional Boron Nitride. *ACS Nano* **2012**, *6*, 7053−7058.
(37) Stebounova, L.; Akhremitchev, B. B.; Walker, G. C. Enhancement of the Weak Scattered Signal in Apertureless Near-Field Scanning Infrared Microscopy. *Rev. Sci. Instrum.* **2003**, *74*, 3670−3674.
(38) Raschke, M. B.; Lienau, C. Apertureless Near-field Optical Microscopy: Tip−Sample Coupling in Elastic Light Scattering. *Appl. Phys. Lett.* **2003**, *83*, 5089−5091.
(39) Keilmann, F.; Hillenbrand, R. Near-Field Microscopy by Elastic Light Scattering from a Tip. *Philos. Trans. R. Soc., A* **2004**, *362*, 787−805.
(40) Cvitkovic, A.; Ocelic, N.; Hillenbrand, R. Analytical Model for Quantitative Prediction of Material Contrasts in Scattering-Type Near-Field Optical Microscopy. *Opt. Express* **2007**, *15*, 8550−8565.
(41) Gomez, L.; Bachelot, R.; Bouhelier, A.; Wiederrecht, G. P.; Chang, S. H.; Gray, S. K.; Hua, F.; Jeon, S.; Rogers, J. A.; Castro, M. E.; Blaize, S.; Stefanon, I.; Lerondel, G.; Royer, P. Apertureless Scanning Near-Field Optical Microscopy: A Comparison between Homodyne and Heterodyne Approaches. *J. Opt. Soc. Am. B* **2006**, *23*, 823−833.
(42) To describe vibrational modes of crystals of long range periodicity, the term "phonon" should be used. However, BNNTs studied here are much smaller than the wavelength of IR light and do not always have translational invariance. Therefore, a more general term "vibrational" is preferred.
(43) Zhi, C. Y.; Bando, Y.; Tang, C. C.; Golberg, D.; Xie, R. G.; Sekigushi, T. Phonon Characteristics and Cathodoluminescence of Boron Nitride Nanotubes. *Appl. Phys. Lett.* **2005**, *86*, 213110.
(44) Lee, C. H.; Wang, J. S.; Kayatsha, V. K.; Huang, J. Y.; Yap, Y. K. Effective Growth of Boron Nitride Nanotubes by Thermal Chemical Vapor Deposition. *Nanotechnology* **2008**, *19*, 455605.
(45) The tube has a diameter larger than 50 nm, whereas the vertical field localization at the tip apex is about 10 nm (see Supporting Information). Therefore, the image dipole of BN vibrations in the gold substrate is weak and is not expected to provide enough signal for destructive interference under the polarization of light.
(46) Celik-Aktas, A.; Zuo, J. M.; Stubbins, J. F.; Tang, C. C.; Bando, Y. Double-Helix Structure in Multiwall Boron Nitride Nanotubes. *Acta Crystallogr., Sect. A* **2005**, *61*, 533−541.
(47) Kukovitsky, E. F.; L'Vov, S. G.; Sainov, N. A. VLS-Growth of Carbon Nanotubes from the Vapor. *Chem. Phys. Lett.* **2000**, *317*, 65−70.
(48) Kukovitsky, E. F.; L'Vov, S. G.; Sainov, N. A.; Shustov, V. A.; Chernozatonskii, L. A. Correlation between Metal Catalyst Particle Size and Carbon Nanotube Growth. *Chem. Phys. Lett.* **2002**, *355*, 497−503.
(49) The multiwall of BNNT forms a concentric cylindrical capacitor. Spacing variations between walls correspond to different local capacitances, which determine their ability to hold electrons during the SEM measurement.
(50) The data acquisition rate of the pseudo-heterodyne method is determined by the slower modulation rate of its double modulations. For example, with a tip tapping frequency at 150 kHz and reference mirror modulation frequency at 5kHz, the acquisition rate is determined by the slower 5 kHz which corresponds to a long lock-in time constant. The data acquisition rate of our method is the same as a typical *a*NSOM determined by the tip oscillation frequency of 150 kHz, which allows a 30 times shorter lock-in time constant.